Geophys. J. Int. (2026) **2026**, 1–19

Uniform automated analysis of S_{diff} splitting due to lowermost mantle anisotropy: Caveats and curated global dataset

Alex Sun[1], Jonathan Wolf*[1,2,3], Barbara A. Romanowicz[1], Ed Garnero[4], John D. West[4]

[1] *Department of Earth and Planetary Science, University of California, Berkeley, CA, USA*

[2] *Miller Institute for Basic Research in Science, Berkeley, CA, USA*

[3] *Department of Earth and Planetary Sciences, University of California, Santa Cruz, CA, USA*

[4] *School of Earth and Space Exploration, Arizona State University, Tempe, AZ, USA*

SUMMARY

Seismic anisotropy, the dependence of seismic wave speeds on the direction of propagation and/or polarization, places crucial constraints on deformation and convective flow in the lowermost mantle (the D″ layer). Shear waves that diffract along the core-mantle boundary (CMB) are ideally suited for probing this region due to their long horizontal ray paths in the lowermost mantle. However, the inference of D″ anisotropy presents multiple methodological challenges, including the need for accurate upper mantle corrections and the potential for apparent splitting produced by isotropic structures. In this study, we leverage global wavefield simulations to develop an automated measurement procedure that excludes S_{diff} waves that are strongly SV_{diff}-polarized, which can lead to apparent splitting even in the absence of seismic anisotropy. We apply this workflow to a global dataset of $\sim$20 million three-component seismograms. By adhering to strict quality control criteria, we generate a highly regionally consistent dataset of high-confidence measurements. Overall, we obtain $\sim 4,300$ S_{diff} splitting measurements that constrain the presence or absence of D″ anisotropy. We project these measurements onto the D″ layer and report S_{diff} splitting across 237 global geographic bins (approximately 28 per cent of the D″ layer by surface area) with sufficient data coverage. Of these, 55 bins exhibit clear splitting, many of which are located beneath the northern Pacific. Furthermore, we characterize the directional dependence of splitting using a backazimuth binning algorithm for regions with multi-directional coverage. We make this curated dataset of geographically and directionally

binned S_{diff} splitting measurements, along with all codes necessary to reproduce it, publicly available.

Key words: Seismic anisotropy – Dynamics: convection currents, and mantle plumes – D″ – Mantle processes

1 INTRODUCTION

Seismic anisotropy, defined as the dependence of seismic wave speeds on propagation and/or polarization direction, provides insights into deformation induced by convective flow, constraints that are challenging to obtain otherwise (e.g., Nowacki et al. 2011; Long & Becker 2010; Romanowicz & Wenk 2017; Wolf et al. 2024a). Earth's mantle is seismically anisotropic, particularly within the upper mantle (e.g., Long & Becker 2010; Montagner 1998; Romanowicz & Wenk 2017; Hansen et al. 2021), the lowermost mantle (e.g., Nowacki et al. 2011; Romanowicz & Wenk 2017; Nowacki & Cottaar 2021; Wolf et al. 2024a; Wookey et al. 2005), also referred to as D″, and possibly the transition zone (e.g., Yuan & Beghein 2014; Chang & Ferreira 2019). In contrast, the bulk of the lower mantle appears nearly isotropic (e.g., Niu & Perez 2004; Meade et al. 1995), although seismic anisotropy has been detected in the uppermost lower mantle near subduction zones (e.g., Foley & Long 2011; Mohiuddin et al. 2015; Ferreira et al. 2019).

As S waves bottom deeper in the mantle with increasing epicentral distance, their bottoming depth eventually reaches the core-mantle boundary at an epicentral distance of approximately 100°. Beyond this distance, the wave can no longer turn back through the mantle and instead propagates along the CMB as a diffracted shear wave, or S_{diff} (Figure 1c). Throughout this study, we identify S_{diff} arrivals using theoretical travel times computed for a one-dimensional reference Earth model. Upon diffraction, direct S and ScS become asymptotic, but have approximately opposite SV polarities, leading to destructive interference, the details of which depend on lowermost mantle velocity, velocity gradient, and attenuation (e.g., Ritsema et al. 1997; Komatitsch et al. 2010; Borgeaud et al. 2016; Parisi et al. 2018). Owing to their long diffraction paths along the CMB, they are highly sensitive to lowermost mantle structure, including D″ anisotropy. Due to this strong sensitivity to seismic anisotropy, they have been used in numerous previous regional lowermost mantle anisotropy analyses (e.g., Vinnik et al. 1989a; Lay & Young 1991; Vinnik et al. 1998; Ritsema et al. 1998; Wysession et al. 1999; Cottaar & Romanowicz 2013; Wolf & Long 2023).

Despite their strong sensitivity to lowermost mantle structure and seismic anisotropy, global wavefield simulations have revealed that travel-time differences between SH- and SV-polarized S_{diff} waves can accumulate even in isotropic structures, a finding reproduced in multiple wavefield simulation studies (e.g., Komatitsch et al. 2010; Parisi et al. 2018; Borgeaud et al. 2016; Wolf et al. 2023a). We note that the magnitude of these apparent travel-time differences is period-dependent and varies with the specific velocity structure encountered along the diffracted path. These studies corroborated earlier work highlighting the importance of the D″ velocity gradient (Ritsema et al. 1997) and further demonstrated the influence of interfering phases (Komatitsch et al. 2010), three-dimensional velocity structure (Parisi et al. 2018), and seismic attenuation (Borgeaud et al. 2016). While these investigations focused on differential travel times, subsequent work showed that

⋆ jonathan.wolf@berkeley.edu

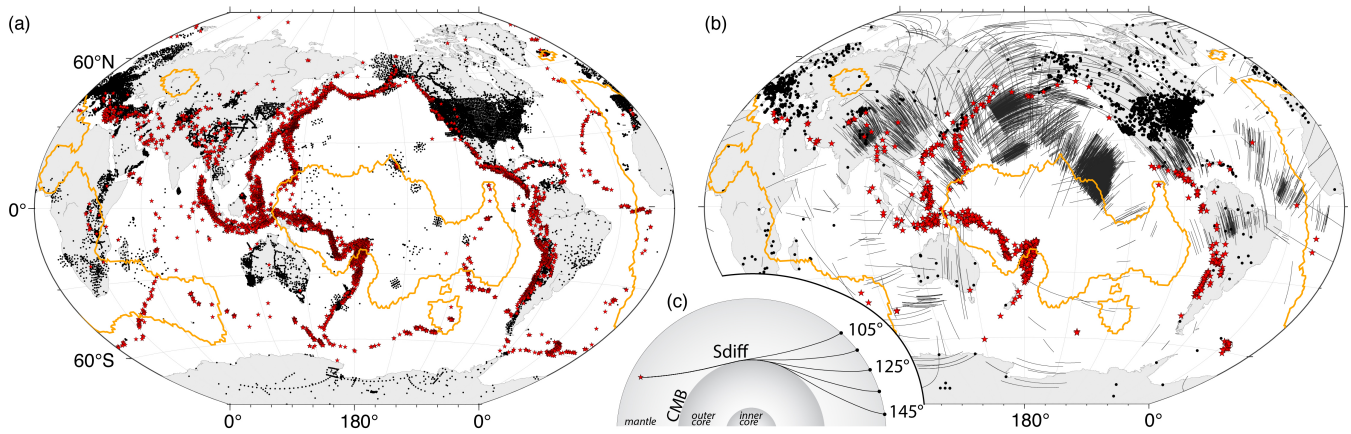

Figure 1. Overview of the ADEPT dataset and S_{diff} raypath coverage. (a) Global distribution of all seismic stations (black circles) and earthquakes (red stars) in the ADEPT database. (b) Earthquakes (red stars) and stations (black circles) that yielded usable S_{diff} splitting measurements, together with the corresponding CMB raypath segments (gray lines). In both panels, low velocity regions derived from a cluster analysis (Lekic et al. 2012) (where 3 out of 5 tomography models indicate low velocities) are shown as orange outlines. (c) Schematic cross-section of the Earth illustrating S_{diff} raypaths at multiple epicentral distances.

explicit shear-wave splitting measurements, which impose strict requirements on waveform shape (e.g., Vinnik et al. 1984; Silver & Chan 1991), can mitigate the misidentification of seismic anisotropy if certain conditions are met (Wolf et al. 2023a).

Extensive global compilations exist for upper mantle anisotropy, as detected with SKS splitting (e.g., Barruol et al. 2009; Becker et al. 2012; Trabant et al. 2012; Liu et al. 2014; Walpole et al. 2014; Wolf et al. 2025, 2026); however, uniform global analyses of lowermost mantle anisotropy are rare and have not yet been applied to S_{diff}. In this study, we apply a rigorous, wave-simulation-informed quality control workflow to a dataset of ∼20 million seismograms, and isolate robust S_{diff} splitting measurements due to D″ anisotropy. This work constitutes one step of a broader initiative to deliver uniformly processed, high-fidelity seismic observables to the community, in the hope that it will fuel new research into Earth dynamics.

2 DATA

We draw upon the ADEPT dataset (`http://www.adept.science`; Figure 1), which aggregates available seismic data from 27 global data centers recorded since 1995 January 1, including all seismic events with moment magnitudes $M_W \geq 5.8$. To date, the collection encompasses over 6,300 earthquakes and more than 20 million three-component seismograms, providing broad global coverage. We apply a standardized pre-processing workflow to all data: two-hour waveform segments are deconvolved to displacement to remove the instrument response, rotated into the vertical, radial, and transverse (ZRT) coordinate system, and downsampled to 20 samples per second.

3 AUTOMATED SHEAR-WAVE SPLITTING MEASUREMENTS

We employ SplitRacerAUTO (Reiss & Rümpker 2017; Link et al. 2022) to automatically measure shear-wave splitting of the S_{diff} phase. Our workflow utilizes the energy-minimization technique of (Silver & Chan 1991), incorporating the corrected uncertainty formulation of Walsh et al. (2013). Because S_{diff} is dominantly SH-polarized, shear-wave splitting transfers energy onto the radial (SV) component; we therefore minimize the radial-component energy to retrieve the splitting parameters. This is directly analogous to the transverse-energy minimization classically applied to the SV-polarized SKS phase, for which the technique was originally developed, with the roles of the

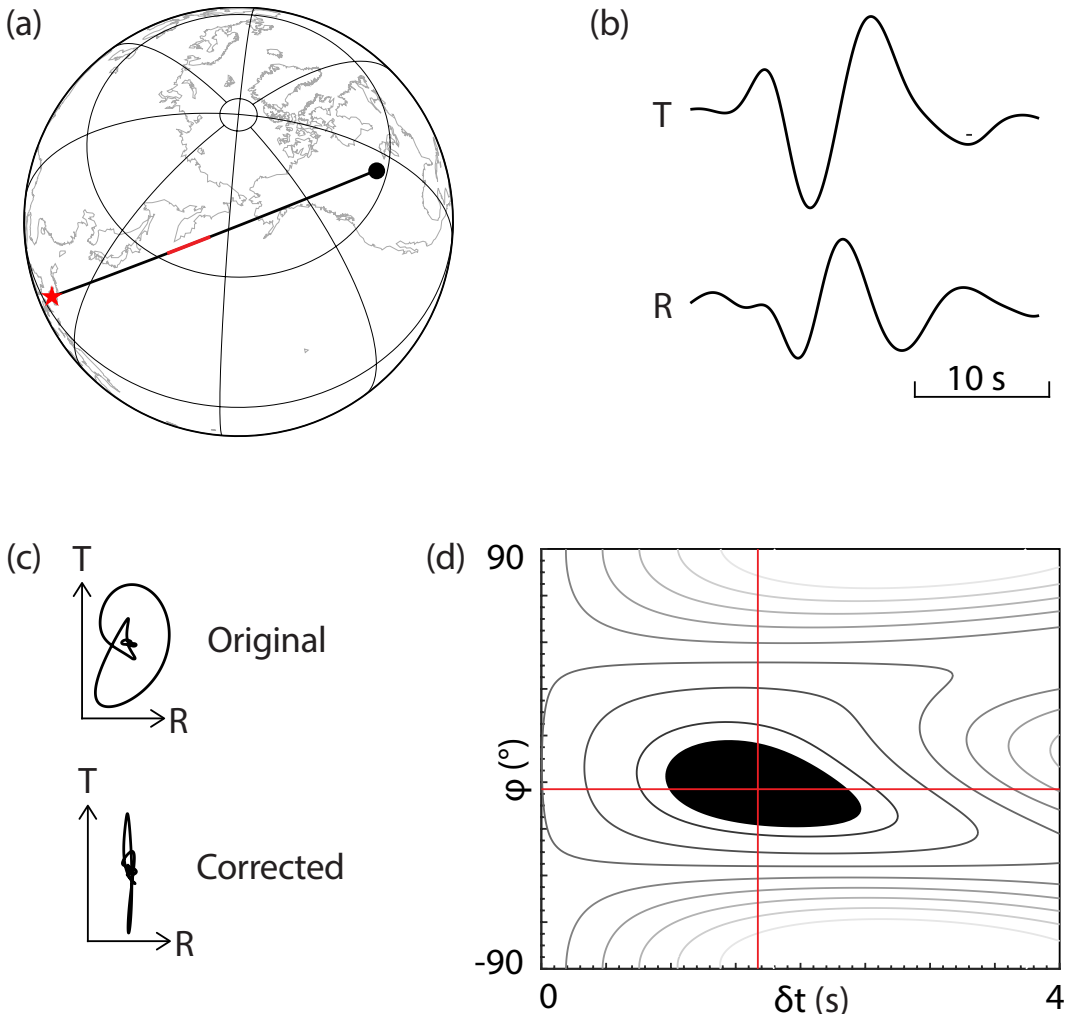

Figure 2. Example S_{diff} splitting measurement for the M_W 6.6, 620-km-deep earthquake of 2009 October 4 (10:58 UTC; 6.74°N, 123.378°E), recorded at station A29A (network TA; 48.92°N, 99.23°W) at an epicentral distance of approximately 113°. (a) Source-receiver geometry: the black line marks the great-circle path connecting the earthquake (red star) and station (black circle), and the red segment along this path highlights the S_{diff} diffracted portion at the CMB, here sampling the lowermost mantle beneath the northwestern Pacific. (b) Transverse (T) and radial (R) component displacement seismograms, bandpass-filtered between 6 and 25 s and normalized, showing the S_{diff} waveform. (c) Particle motion diagrams before (top) and after (bottom) correction for splitting; successful correction linearizes the particle motion. (d) Energy grid search over fast-axis azimuth (ϕ) and delay time (δt), with the black region indicating the 95% confidence interval of the best-fit splitting parameters.

radial and transverse components reversed. We determine three splitting parameters: the fast polarization direction ϕ' (measured relative to the backazimuth) (Nowacki et al. 2010), the delay time δt between the fast and slow shear-wave components, and the splitting intensity SI (Chevrot 2000). Crucially, we restrict our S_{diff} splitting measurements to seismograms where the phase is sufficiently SH-polarized immediately following its diffraction at the CMB (as detailed in Section 4). This allows us to assume that significant energy on the radial (SV) component arises primarily from splitting. Under this assumption of dominant SH energy, the splitting intensity for S_{diff} can be defined as:

$$SI = -2\frac{R(t)T'(t)}{|T'(t)|^2} \tag{1}$$

where $R(t)$ denotes the radial component and $T'(t)$ represents the time derivative of the transverse component. We calculate these parameters across 30 time windows surrounding the automatically determined S_{diff} arrival (Link et al. 2022), applying a bandpass filter between 6 and

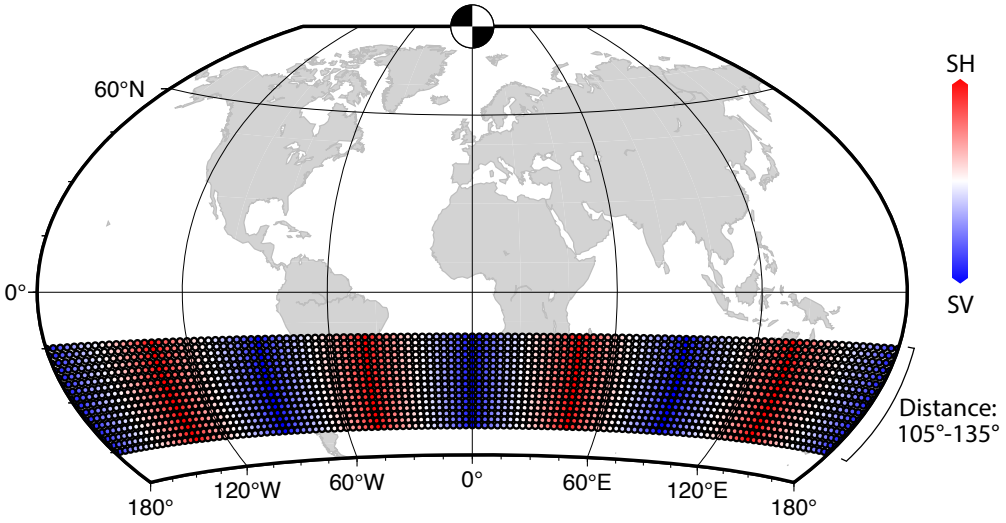

Figure 3. Source-receiver geometry for synthetic tests. A strike-slip source (beachball) is centered at the North Pole, producing azimuth-dependent source-polarizations (indicated by the color scale). Stations (colored circles) are distributed at epicentral distances of 105°–135°. Note that for S_{diff}, SV-wave energy is lowered upon diffraction, an effect that is not represented by the color scale.

25 s, a period band commonly used in shear-wave splitting analyses (e.g., Long & Silver 2009). To ensure robustness, we retain only those measurements that SplitRacerAUTO's automated quality-control assessment classifies as stable across these windows (Link et al. 2022), based on the consistency of the windowed splitting estimates. An example S_{diff} splitting measurement is shown in Figure 2.

The reliable application of explicit corrections for upper mantle anisotropy has been shown to be challenging, especially for S_{diff} waves (e.g., Wolf et al. 2022, 2023a). Therefore, to distinguish effects of upper and lowermost mantle anisotropy, we select a conservative approach and retain only S_{diff} splitting measurements that satisfy one of two criteria: (1) for each S_{diff} measurement, we find the SKS or SKKS (collectively, $*$KS) measurement recorded at the same station (for any event) with the most similar backazimuth; if this nearest $*$KS measurement lies within 3° backazimuth of the S_{diff} observation and is classified as a null measurement, the S_{diff} measurement is retained, or (2) the recording station is classified as a null station in the global $*$KS splitting compilation of (Wolf et al. 2025), which is based on a previous version of the same large dataset.

4 DEVELOPMENT OF AN AUTOMATED PROCESSING WORKFLOW

To develop a robust automated processing workflow for S_{diff} splitting measurements, we conduct global wavefield simulations. Such numerical experiments have been crucial in previous studies for identifying limitations in S_{diff} splitting analysis, demonstrating how isotropic structures can produce artifacts that potentially mimic anisotropy (e.g., Komatitsch et al. 2010; Borgeaud et al. 2016; Parisi et al. 2018). While a rigorous workflow was previously proposed to identify and avoid these pitfalls (Wolf et al. 2023a), it relied on manual assessment steps that were not easily translated into an automated process. In this study, we build upon the reliability criteria of that prior work but re-engineer the methodology into a fully automated algorithm suitable for applying to massive, global datasets.

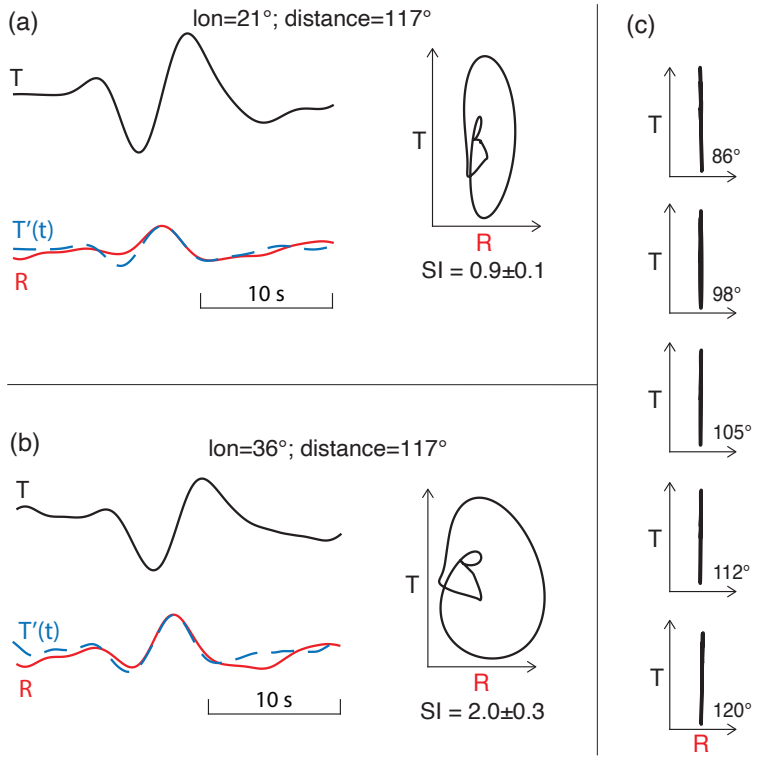

Figure 4. (a,b) Apparent splitting induced by source polarization in an isotropic Earth model (PREM). Synthetic S_{diff} waveforms are shown for an epicentral distance of 117° at two backazimuths. Seismograms display transverse ($T(t)$, black), radial ($R(t)$, red), and transverse time-derivative ($T'(t)$, blue) components, along with particle motion diagrams (radial vs. transverse amplitude). (a) Longitude 21°: Mixed SH/SV polarization from the source mechanism causes apparent splitting ($SI = 0.9 \pm 0.1$) without anisotropy. (b) Longitude 36°: Stronger SV contamination significantly increases the apparent splitting ($SI = 2.0 \pm 0.3$). (c) Null polarization (linear T-component motion) for a pure SH wave for synthetics through the tomography model S40RTS. These synthetic simulations demonstrate the need to filter by amplitude ratio to isolate predominantly SH-polarized arrivals.

4.1 Global wavefield simulations

We conduct global wavefield simulations using the spectral-element solver AxiSEM3D (Leng et al. 2016, 2019; Fernando et al. 2024), computing synthetic seismograms down to a period of 5 s. As the background model, we always use the isotropic version of the Preliminary Reference Earth Model (PREM, Dziewonski & Anderson 1981), incorporating Earth's ellipticity and PREM-attenuation. In some simulations, we replace the PREM-mantle with the seismic tomography model S40RTS (Ritsema et al. 2011) to investigate effects of 3D velocity structure. For our simulations, we always use a strike-slip earthquake at 500 km depth, located at the North Pole (Figure 3). By placing stations at epicentral distances between 105° and 135° (Figure 3), and at all azimuths in 1° spacing, we ensure the recording of S_{diff} seismograms with a wide variety of initial polarizations, ranging from fully SH to fully SV, and a large range of epicentral distances (Figure 3). This sampling of the full polarization range is intentional: it is precisely what allows us to characterize apparent splitting and to validate the *ampdiff* criterion, and is the reason we adopt a strike-slip source, rather than to optimize SH or SV radiation for any individual path. For simulations through 1D velocity models, it is sufficient to only cover a 90° azimuthal range due to the repeating source polarization pattern, while for the 3D mantle model we are explicitly interested in the effects of different velocity structures, including raypaths through fast and slow mantle regions, which is why we use the full (0° to 359°) azimuthal range. We utilize wavefield learning (Leng et al. 2019) to adapt the Fourier expansion order of the wavefield in the azimuthal direction, ensuring accurate wave propagation through the 3D tomography model.

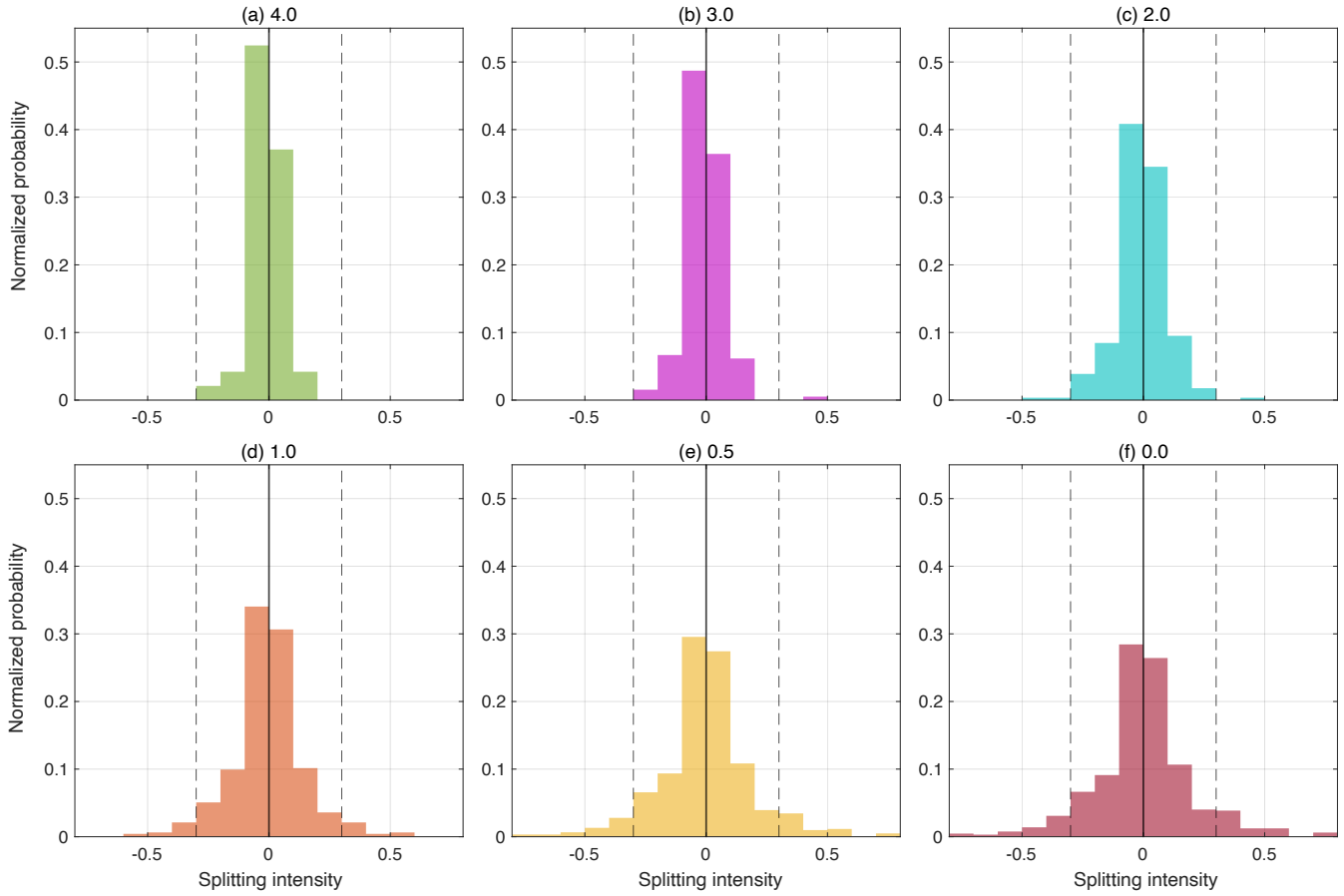

Figure 5. Distribution of splitting intensity (SI) for synthetic S_{diff} measurements computed through the three-dimensional, isotropic (anisotropy-free) velocity model S40RTS, shown as a function of the amplitude ratio threshold (*ampdiff*) between the S_{diff} transverse component and the radial component of SKS or SKKS. Each panel displays the SI histogram for measurements with an *ampdiff* above the indicated threshold: (a) 4.0, (b) 3.0, (c) 2.0, (d) 1.0, (e) 0.5, and (f) 0.0. Ideally, for an isotropic model, the SI should be exactly zero. Higher *ampdiff* thresholds yield tighter distributions centered on zero, whereas lower thresholds introduce spurious apparent splitting from SV-polarized arrivals. Dashed lines indicate $SI = \pm 0.3$, a threshold below which splitting is typically classified as null (e.g., Wolf et al. 2023b).

4.2 Example of apparent S_{diff} splitting in the absence of seismic anisotropy

We present two examples of synthetic waveforms that mimic shear-wave splitting, despite being computed for isotropic PREM (Figure 4a,b). In both instances, the radial component resembles the time derivative of the transverse component, and particle motions are distinctively elliptical. Accordingly, the measured SI values are tightly constrained, quantitatively confirming the initial visual impression. A key feature shared by both examples is that the incident wave is substantially SV-polarized. In contrast, SH-polarized S_{diff} waves traversing even complex 3D velocity structures remain purely SH-polarized at large distances, provided no seismic anisotropy is introduced (Figure 4c). These results corroborate previous findings of apparent S_{diff} splitting in waves of mixed polarization (e.g., Komatitsch et al. 2010; Borgeaud et al. 2016; Parisi et al. 2018; Wolf et al. 2023a). However, they also imply that S_{diff} waves remain a viable probe for D″ anisotropy if they are sufficiently SH-polarized, as the generation of apparent splitting artifacts is fundamentally dependent on the presence of initial SV energy.

4.3 Polarization constraints for reliable S_{diff} splitting measurements

The polarization of the S_{diff} -wave particle motion at each station is determined from its principal axis of motion, the eigenvector of the covariance matrix with the largest eigenvalue (Silver & Chan 1991). For S_{diff} waves that are truly SH-polarized at the source, any observed

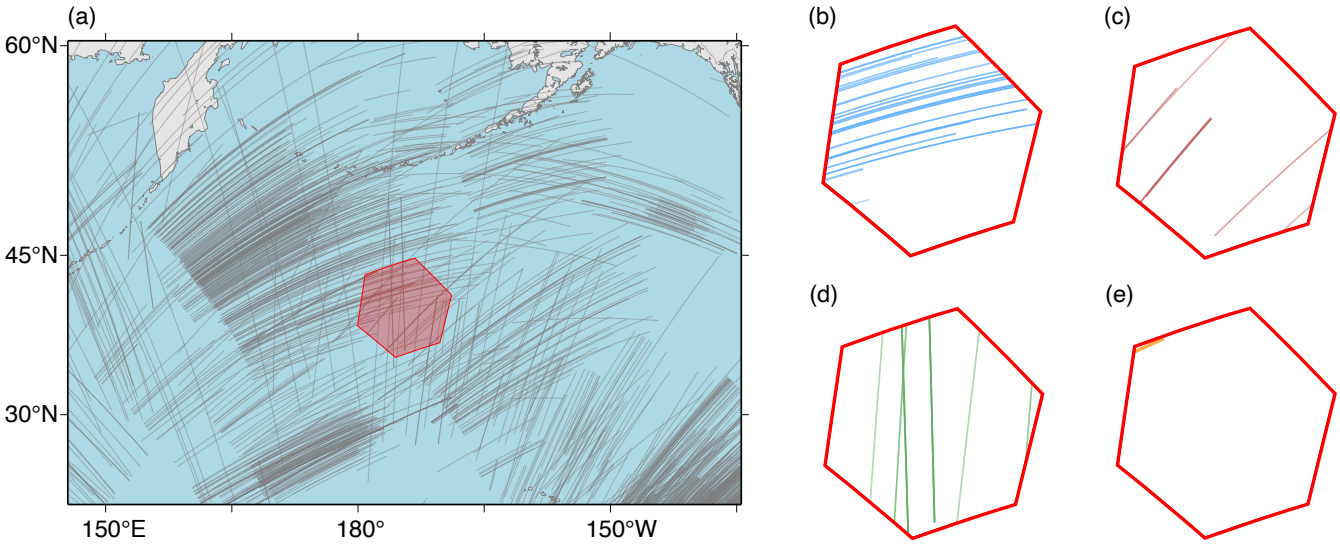

Figure 6. Illustration of the geographic and directional binning scheme. (a) All S_{diff} raypaths (gray lines) around an example hexagon H at the CMB. (b–e) Individual cells (H, b) for different propagation azimuth bins b. Each cell groups measurements traveling in similar directions through the hexagon, enabling characterization of directional dependence of splitting.

SV energy should primarily result from shear-wave splitting; consequently, the dominant polarization vector must remain aligned with the transverse component. We emphasize that this does not contradict the apparent splitting described above (Figure 4): isotropic structure produces spurious SV energy only when the incident wave is already partly SV-polarized, whereas a wave that is genuinely SH-polarized upon diffraction acquires SV energy only in the presence of true anisotropy (Figure 4c). The criterion below is designed precisely to retain such genuinely SH-polarized waves. Based on this physical expectation, we apply a strict selection criterion to both synthetic and real data: we restrict our analysis to S_{diff} waves where the polarization direction inferred from the covariance matrix deviates by no more than $\pm 10^{\circ}$ from the theoretical SH polarization direction.

As a simple waveform-based proxy for the relative SV-SH polarization, we additionally compute a parameter we term *ampdiff*, defined as the ratio of the peak transverse-component amplitude of S_{diff} to the peak radial-component amplitude of the reference $*$KS phase:

$$\text{ampdiff} = \frac{\max_t |T(t)|}{\max_t |R_{*\text{KS}}(t)|}, \tag{2}$$

where $T(t)$ is the transverse component of the S_{diff} waveform, $R_{*\text{KS}}(t)$ is the radial component of the reference $*$KS phase (SKS for epicentral distances $< 115^{\circ}$, SKKS otherwise), and the maxima are evaluated over the respective measurement windows. While this ratio is subject to minor modulation by source radiation patterns (due to slightly different takeoff angles for S_{diff} and $*$KS) and path-dependent anisotropy, it generally provides a robust and efficient estimate of the relative SH-SV energy balance for the S_{diff} raypath. We validate the utility of this proxy using synthetic seismograms in the subsequent section and include the *ampdiff* value for every measurement in our public dataset, enabling users to independently select thresholds appropriate for their specific objectives. We further explore the influence of the *ampdiff* parameter on our real-data measurements in Section 6.

To investigate the influence of the *ampdiff* parameter, we measure shear-wave splitting for all S_{diff} phases in our synthetic simulation, which incorporates the S40RTS tomography model and a station distribution spanning all longitudes (Figure 3). We restrict our analysis to S_{diff} phases that satisfy the previously described polarization criteria, recording the *ampdiff* value for each valid measurement. Generally, a higher *ampdiff* corresponds to a more strongly SH-polarized S_{diff} wave, thereby minimizing the risk of apparent splitting. Figure 5 illustrates

the distributions of the splitting intensity (SI) for synthetic results for varying *ampdiff* values. We adopt the convention that $|SI| < 0.3$ represents a null or near-null measurement (e.g., Wolf et al. 2025). For *ampdiff* $\geq$ 2, significant splitting ($|SI| \geq 0.3$) occurs in fewer than 2% of cases. However, the proportion of false splitting measurements, identified despite the absence of anisotropy, rises substantially at *ampdiff* < 2. We therefore conclude that *ampdiff* ≥ 2 serves as a robust threshold to ensure the reliability of our real-data S_{diff} splitting measurements. Importantly, while *ampdiff* ≥ 2 indicates that the transverse-component S_{diff} amplitude is at least twice as large as the radial-component $*$KS amplitude, this does not imply that the S_{diff} phase possesses significant SV energy (i.e., up to half the amplitude of the transverse component) at the onset of diffraction. This is because the radial components of the S and ScS phases have opposite polarities and destructively interfere.

5 GEOGRAPHIC AND DIRECTIONAL BINNING

To organize our S_{diff} splitting measurements into geographic bins, we discretize the CMB using the H3 hierarchical spatial indexing system (Brodsky 2018) at resolution 1, yielding hexagonal regions with an edge length of approximately 400 km. This size results in roughly 840 hexagonal tiles over the entire CMB. Each S_{diff} raypath can sample multiple hexagons along the CMB; we assign fractional weights $W_{m,H}$ according to the proportion of the raypath falling within each hexagon H, ensuring $\sum_H W_{m,H} = 1$ for each measurement m. The raypath segment is determined by the start and end points of CMB diffraction. Because the length of this diffracted segment grows with epicentral distance, S_{diff} phases recorded at shorter distances sample fewer hexagons than those recorded at larger distances; the fractional weighting $W_{m,H}$ accounts for this when assessing cell coverage, but a mild distance-dependent sampling bias remains.

Splitting of S_{diff} depends not only on where along the CMB the wave samples the anisotropic structure, but also on the azimuthal direction in which it propagates through that structure. We therefore further group measurements by local propagation azimuth into 24 intervals of 15° width (0°, 15°, 30°, ..., 345°). We retain the full 0°–360° range rather than folding azimuths separated by 180° onto one another, because the fast-axis direction ϕ' (measured relative to backazimuth) depends on the actual propagation direction; measurements sampling a cell from azimuths 180° apart therefore cannot be assumed to yield equivalent splitting. Each (hexagon H, propagation azimuth b) pair defines a *cell*, the unit we use for our geographic and directional organization.

We classify cells based on data coverage and measurement type. Cells with insufficient data (total raypath weight < 1.0) are excluded from analysis. For cells with sufficient coverage, individual measurements are classified as "null" or "split" based on the SplitRacerAUTO quality assessment, and we perform a weighted majority vote to classify each cell accordingly. Once a cell is classified, we retain only the measurements consistent with that classification: split measurements are removed from null cells, and null measurements are removed from split cells. This ensures that the signal within each cell is internally consistent and that subsequent analyses are not contaminated by outlier measurements of the opposite type (Figure 6).

6 RESULTS

After applying all quality control criteria described in the preceding sections, we retain a total of 5,797 individual S_{diff} splitting measurements at a minimum threshold of *ampdiff* ≥ 1. Restricting the dataset to *ampdiff* ≥ 2, a threshold that our synthetic tests indicate effectively

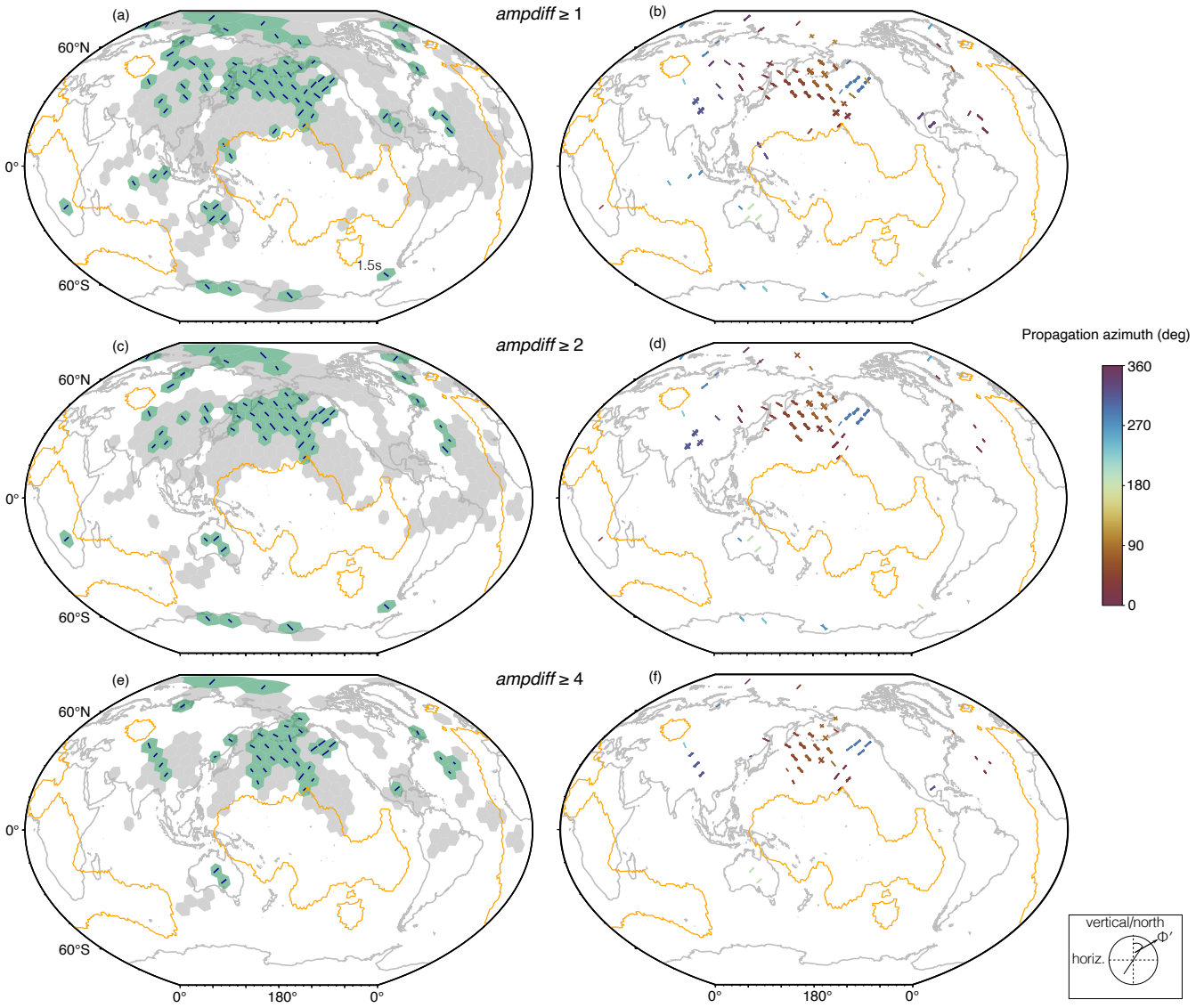

Figure 7. Summary of S_{diff} splitting results for minimum *ampdiff* thresholds of 1 (top row), 2 (middle row), and 4 (bottom row). (a, c, e) Stickograms projected onto the CMB, displaying fast-axis direction (ϕ') and delay-time (δt) measurements from the dominant split azimuth (legend). Within each split hexagon (green), a single stick represents the directional cell with the maximum absolute splitting intensity: orientation denotes the weighted circular mean of ϕ', while length is proportional to the weighted mean of δt. Gray hexagons indicate null classifications. (b, d, f) Individual measurements from split directional cells. Stick orientation indicates ϕ', length is proportional to δt, and color represents the propagation azimuth (see legend).

suppresses spurious apparent splitting, leaves 4,320 measurements. At the most conservative threshold of *ampdiff* ≥ 4, the dataset is further reduced to 1,870 measurements. Consequently, when applying our hexagonal binning scheme, the resulting geographical coverage is highly dependent on the chosen *ampdiff* threshold. We present the spatial distributions for all three *ampdiff* thresholds in Figure 7. At our preferred threshold of *ampdiff* ≥ 2, these measurements provide sufficient coverage in 237 hexagonal bins, corresponding to approximately 28 per cent of the D″ layer by surface area, of which 55 are classified as split (Figure 7c).

We project all (ϕ', δt) measurements onto the CMB in the form of "stickograms" (see the legend in Figure 7). We classify a given hexagonal bin as "split" if at least one of its directional cells exhibits splitting, and as "null" only if all of its directional cells yield null measurements (Figure 7a, c, e). For the split bins, we plot a single representative (ϕ', δt) stick corresponding to the directional cell with the maximum absolute splitting intensity. Because measurements satisfying *ampdiff* ≥ 4 provide the highest confidence, the spatial distribution

derived from this subset serves as a benchmark for evaluating results obtained at lower *ampdiff* thresholds. Overall, the splitting parameters exhibit high consistency across all evaluated *ampdiff* thresholds (Figure 7a, c, e).

To characterize the directional dependence of splitting, Figure 7(b,d,f) display all individual (ϕ', δt) measurements from the split directional cells, color-coded by local propagation azimuth. As the *ampdiff* threshold increases, the scatter within each propagation direction noticeably decreases. This trend highlights the effectiveness of the *ampdiff* criterion in isolating higher-quality measurements.

7 DISCUSSION

7.1 Inferring seismic anisotropy from S_{diff} waves

In our synthetic tests, approximately 65% of the data yield *ampdiff* values below 2, which can potentially induce apparent splitting (Section 4.3), as shown in Figure 4. Constraints from real data (Figure 7) demonstrate that these low *ampdiff* values noticeably impact the spread of S_{diff} measurements and, consequently, the reliability of individual observations. Furthermore, when all *ampdiff* values are retained in synthetics produced for an isotropic Earth, significant apparent splitting occurs in roughly 15% of the measurements (Figure 5). These effects are largely mitigated when a threshold of *ampdiff* ≥ 2 is applied.

This study tests the effect of different source polarizations (particularly, *ampdiff* values) on shear-wave splitting measurements derived from S_{diff} phases and implements an automated procedure to mitigate potential contamination. Such shear-wave splitting measurements place strict requirements on waveform shape (e.g., Vinnik et al. 1989b; Silver & Chan 1991). While some previous S_{diff} studies implement such explicit splitting measurements (e.g., Wolf & Long 2022; Wolf et al. 2024b), the majority have relied on measuring the relative time delay of SH_{diff} relative to SV_{diff} (e.g., Vinnik et al. 1995; Garnero & Lay 1997; Pulliam & Sen 1998; Vinnik et al. 1998; Fouch et al. 2001). Our synthetic tests do not explicitly address the reliability of these past differential travel-time measurements, which do not consider the shape of the radial and transverse S_{diff} waveforms. In contrast, our own measurements are explicit waveform-splitting measurements obtained with a uniformly applied, quality-controlled processing workflow (Wolf et al. 2025), and therefore directly assess the shape of the radial and transverse S_{diff} waveforms.

7.2 Global S_{diff} measurements in the context of previous literature

As illustrated in Figure 8, our automated measurement procedure significantly expands the geographical footprint of S_{diff} splitting observations. We approximately triple the total area of the lowermost mantle previously analyzed by studies combining differential SH_{diff} –SV_{diff} travel times and actual waveform splitting measurements. When compared strictly to previous literature that employs explicit (ϕ, δt) splitting measurements, our dataset encompasses an area nearly an order of magnitude larger. This coverage allows us to evaluate D$''$ anisotropy on a broader, more continuous scale, bridging gaps between previously isolated regional studies.

Furthermore, our catalog systematically reports both split and "null" measurements. Previous investigations of D$''$ anisotropy using S_{diff} phases have predominantly published split measurements, leaving null measurements underreported. However, null observations, indicating an absence of observable splitting from a particular direction, are vital for accurately constraining mantle deformation. They provide essential evidence for either intrinsically isotropic regions or specific sampling geometries in which the initial polarization aligns with the apparent

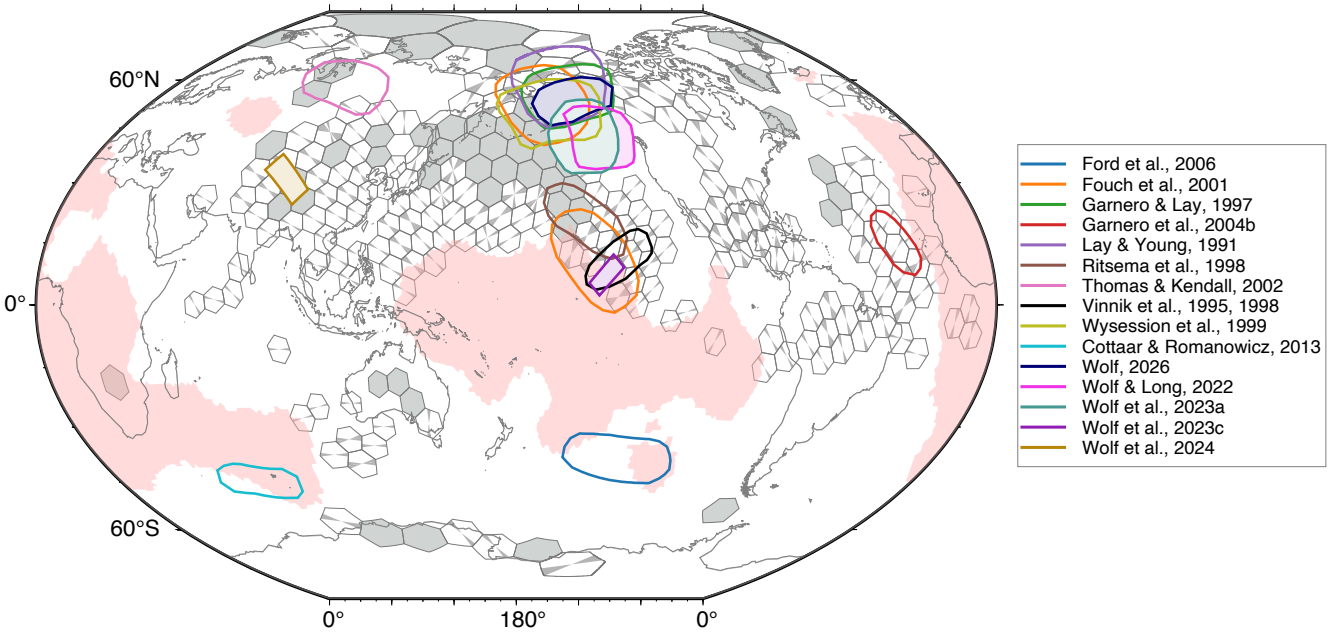

Figure 8. Distribution of S_{diff} splitting measurements obtained in this study compared to the regional coverage of all previous S_{diff} anisotropy studies Lay & Young (1991); Vinnik et al. (1995, 1998); Garnero & Lay (1997); Ritsema et al. (1998); Wysession et al. (1999); Fouch et al. (2001); Thomas & Kendall (2002); Ford et al. (2006); Cottaar & Romanowicz (2013); Wolf & Long (2022); Wolf et al. (2023a); Wolf & Long (2023); Wolf et al. (2024b); Wolf (2026). Previously studied regions are shown as colored outlines (legend); studies that report explicit (ϕ', δt) shear-wave splitting measurements are additionally indicated by light shading of these regions in the same color. Light red shading marks regions where at least three of five tomographic models from a cluster analysis (Lekic et al. 2012) indicate low seismic velocities. The gray hexagons underlying the map show the core-mantle boundary sampling of our curated dataset: bins in which we measure strong splitting are filled solid gray, whereas sampled bins without strong splitting are drawn as open hexagons, with a line indicating the propagation direction sampled through the bin.

fast or slow direction of the anisotropic fabric. Because this apparent orientation depends on the ray's incidence angle and backazimuth, nulls are difficult to produce by tilted anisotropy. By including nulls, we mitigate reporting bias and provide a more robust foundation for future inferences.

Radial anisotropy, the discrepancy in seismic wave speeds between horizontally and vertically polarized shear waves, is frequently used to interpret lowermost mantle anisotropy, largely because it can be inferred using global seismic tomography approaches (e.g., French & Romanowicz 2014; Chang et al. 2015; Suzuki et al. 2021). In the parameterization of radial anisotropy, $V_{SV} > V_{SH}$ implies a fast-axis direction of $\phi' = 90^\circ$, whereas $V_{SH} > V_{SV}$ implies $\phi' = 0^\circ$. Our explicit shear-wave splitting measurements are inherently insensitive to both of these end-member scenarios; if the symmetry axes align with the initial polarization, no energy is split to the SV_{diff} component. Consequently, from a practical standpoint, our method is much more likely to detect absolute ϕ' values between 20° and 70°, which are consistently seen in our observations. Cases where ϕ' is near 0° or 90° would simply yield null measurements. Therefore, direct comparisons between our splitting results and global radial anisotropy models are of limited diagnostic value. We note that studies that directly compare the absolute travel times of SH_{diff} and SV_{diff} phases, should these be due to seismic anisotropy, are more directly comparable to maps of radial anisotropy.

Because our measurements are insensitive to certain anisotropy geometries, our classification of null versus split bins is challenging to compare to studies relying on differential SH_{diff} and SV_{diff} travel times; studies analyzing differential travel times may infer seismic anisotropy in locations in which no significant splitting is detected. When compared to studies that explicitly resolve the splitting parameters (ϕ', δt), our results demonstrate strong agreement, with the exception of the central Pacific (Vinnik et al. 1995; Wolf & Long 2023; Kawai &

Geller 2010). However, we note that the reported splitting measurement (Wolf & Long 2023) (as opposed to relative SH_{diff}-SV_{diff} delay time analysis) in this region was near null and inferred only using a single seismic event.

We capture the directional dependence of S_{diff} splitting. While previous studies relying on S_{diff} to infer seismic anisotropy have typically been limited to a single sampling direction for any given region, we bin our measurements based on propagation azimuth (Figures 6 and 7). Resolving this directional variation is important, as it helps to distinguish between different anisotropic symmetries and to accurately map the underlying convective flow fields in the lowermost mantle.

8 CURATED S_{diff} SPLITTING DATASET

We make all global S_{diff} (ϕ', δt) splitting and null measurements publicly available. We provide a `.txt` file in the Supplementary Material that includes the following information for each individual measurement: event name, for example '199501171654', corresponding to an event that occurred on 1995 January 17 at 16:54 UTC; event latitude (°); event longitude (°); event depth (km); station code; network code; station latitude (°); station longitude (°); quality tag (good, average, null-measurement, or poor); δt (s); δt lower 95% confidence bound (s); δt upper 95% confidence bound (s); ϕ' (°); ϕ' lower 95% confidence bound (°); ϕ' upper 95% confidence bound (°); splitting intensity SI; SI lower 95% confidence bound; SI upper 95% confidence bound; *ampdiff* value; and backazimuth (°). We include the *ampdiff* value for every measurement, enabling users to independently select amplitude ratio thresholds appropriate for their specific objectives.

In addition to the individual measurements, we provide the geographically and directionally binned data product as a separate `.txt` file. Each row corresponds to a single (hexagon, propagation-azimuth) cell and includes: hexagon identifier; hexagon center latitude (°); hexagon center longitude (°); propagation-azimuth bin (°, in multiples of 15°); cell classification (split or null); weighted circular mean fast-axis direction ϕ' (°); weighted mean delay time δt (s); and weighted mean splitting intensity SI.

Furthermore, to ensure full reproducibility, we make all codes used for this study publicly available at `https://doi.org/10.5281/zenodo.19664403`. This repository includes the measurement codes, S_{diff} waveform snippets, and the codes used for geographic and directional binning.

9 CONCLUSIONS

In this study, we present the first uniform analysis of lowermost mantle seismic anisotropy using S_{diff} waveform splitting from a global seismic dataset. By applying an automated, wavefield-simulation-informed workflow to a massive dataset of $\sim$20 million three-component seismograms, we obtain approximately 4,300 robust S_{diff} splitting measurements. Projecting these high-quality measurements onto the D$''$ layer, we report data across 237 geographic bins (approximately 28 per cent of the D$''$ layer by surface area), with 55 bins exhibiting clear splitting, although we do not rule out anisotropy in any bin. For these measurements, we circumvent pitfalls related to apparent splitting caused by strong SV energy, as well as uncertainties associated with explicit upper mantle anisotropy corrections. Therefore, our dataset is conservative and highly quality-controlled.

Our compilation expands the analyzed geographical footprint of D$''$ by approximately a factor of three compared to all previous S_{diff} anisotropy studies combined, and by an order of magnitude compared to prior explicit splitting measurements. We systematically

report both split and null measurements, which mitigates reporting bias and provides essential constraints on the geometry of lowermost mantle deformation. Additionally, by characterizing the directional dependence of splitting through backazimuth binning to the fullest extent possible, our dataset overcomes the limitations of single-direction sampling, enabling future studies to better distinguish between more complex anisotropic symmetries.

To ensure full reproducibility, we make the complete dataset, corresponding metadata, and the automated measurement codes publicly available. Because our measurements have been processed uniformly, they are ideally suited for future integration into anisotropic tomography and global geodynamic modeling.

ACKNOWLEDGMENTS

JW was funded by the Miller Institute for Basic Research in Science at UC Berkeley. BAR and JDW received support from the National Science Foundation via grants No. EAR-2054951 and EAR-1853911. EG received support from EAR-1853911. The ADEPT data project was possible due to NSF grant EAR-2348594.

DATA AVAILABILITY

All data used in this study are publicly available and were collected and pre-processed as part of ASU's global data collection and products project (ADEPT; `http://www.adept.science`). Data were collected from the following on-line data centers: AUSPASS (`https://auspass.edu.au/data.html`), BGR (`https://eida.bgr.de/`), CNDC (`https://www.earthquakescanada.nrcan.gc.ca/stndon/CNDC/index-en.php`), Earthscope (`http://service.iris.edu/`), ETH (`https://eida.ethz.ch/`), FNET (`https://www.fnet.bosai.go.jp/top.php?LANG=en`), GEOFON (`https://geofon.gfz-potsdam.de/`) (GFZ Data Services 1993), GeoNet (`https://www.geonet.org.nz/`), GDMS (`https://gdmsn.cwb.gov.tw/`) (Central Weather Bureau 2012), ICGC (`https://www.icgc.cat/en/Ciutada/Explora-Catalunya/Terratremols`), IGN (`http://www.ign.es/`), INGV (`http://cnt.rm.ingv.it/en/webservices_and_software`), IPGP (`http://ws.ipgp.fr/`) (Institut de physique du globe de Paris (IPGP) & École et Observatoire des Sciences de la Terre de Strasbourg (EOST) 1982), KNMI (`http://rdsa.knmi.nl/`), KOERI (`http://www.koeri.boun.edu.tr/new/en`), LMU (`http://erde.geophysik.uni-muenchen.de/`), NCEDC (`https://ncedc.org/`) (UC Berkeley Seismological Laboratory 2014), NIEP (`https://www.infp.ro/`), NOA (`http://bbnet.gein.noa.gr/HL/`), OHPDMC (`http://ohpdmc.eri.u-tokyo.ac.jp/`), ORFEUS (`http://www.orfeus-eu.org/`), RESIF (`https://seismology.resif.fr/`) (RESIF 1995), SCEDC (`https://scedc.caltech.edu/`) (Caltech 2014), SSN (`http://www.ssn.unam.mx/`) (Instituto de Geofísica, Universidad Nacional Autónoma de México, México 2024), TEXNET (`http://rtserve.beg.utexas.edu/`), UIB-NORSAR (`https://eida.geo.uib.no/`), and USP (`https://sismo.iag.usp.br/`). All networks and network citations are included as Supplementary Information, and were derived from the FDSN network code list (`https://fdsn.org/networks/`).

All splitting measurements are available as text files in the Supplementary Material.

CODE AVAILABILITY

SplitRacerAUTO (Link et al. 2022) is available at `https://www.geophysik.uni-frankfurt.de/64002762/Software`. The precise code version that we used to measure splitting is also available at `https://doi.org/10.5281/zenodo.14834413`. All analysis and figure generation code is available at `https://doi.org/10.5281/zenodo.19664403`.

References

Barruol, G., Wuestefeld, A., & Bokelmann, G., 2009. SKS-Splitting-database, *Université de Montpellier, Laboratoire Géosciences*.

Becker, T. W., Lebedev, S., & Long, M. D., 2012. On the relationship between azimuthal anisotropy from shear wave splitting and surface wave tomography, *Journal of Geophysical Research: Solid Earth*, **117**(B1), B01306.

Borgeaud, A. F., Konishi, K., Kawai, K., & Geller, R. J., 2016. Finite frequency effects on apparent S-wave splitting in the D$''$ layer: comparison between ray theory and full-wave synthetics, *Geophysical Journal International*, **207**, 12–28.

Brodsky, I., 2018. H3: A hexagonal hierarchical geospatial indexing system.

Caltech, 2014. Southern California Earthquake Center.

Central Weather Bureau, 2012. Central Weather Bureau Seismographic Network.

Chang, S.-J. & Ferreira, A. M. G., 2019. Inference on Water Content in the Mantle Transition Zone Near Subducted Slabs From Anisotropy Tomography, *Geochemistry, Geophysics, Geosystems*, **20**, 1189–1201.

Chang, S.-J., Ferreira, A. M. G., Ritsema, J., van Heijst, H. J., & Woodhouse, J. H., 2015. Joint inversion for global isotropic and radially anisotropic mantle structure including crustal thickness perturbations, *Journal of Geophysical Research: Solid Earth*, **120**(6), 4278–4300.

Chevrot, S., 2000. Multichannel analysis of shear wave splitting, *Journal of Geophysical Research: Solid Earth*, **105**, 21579–21590.

Cottaar, S. & Romanowicz, B., 2013. Observations of changing anisotropy across the southern margin of the African LLSVP, *Geophysical Journal International*, **195**, 1184–1195.

Dziewonski, A. M. & Anderson, D. L., 1981. Preliminary reference Earth model, *Physics of the Earth and Planetary Interiors*, **25**, 297–356.

Fernando, B., Wolf, J., Leng, K., Nissen-Meyer, T., Eaton, W., Styczinski, M., Walker, A., Craig, T., Muir, J., Nunn, C., & Long, M., 2024. Axisem3d - an introduction to using the code and its applications, *EarthArXiv*.

Ferreira, A., Faccenda, M., Sturgeon, W., Chang, S.-J., & Schardong, L., 2019. Ubiquitous lower-mantle anisotropy beneath subduction zones, *Nature Geoscience*, **12**, 301—-306.

Foley, B. J. & Long, M. D., 2011. Upper and mid–mantle anisotropy beneath the Tonga slab, *Geophysical Research Letters*, **38**.

Ford, S. R., Garnero, E. J., & McNamara, A. K., 2006. A strong lateral shear velocity gradient and anisotropy heterogeneity in the lowermost mantle beneath the southern pacific, *Journal of Geophysical Research: Solid Earth*, **111**(B3), B03306.

Fouch, M. J., Fischer, K. M., & Wysession, M. E., 2001. Lowermost mantle anisotropy beneath the Pacific: Imaging the source of the Hawaiian plume, *Earth and Planetary Science Letters*, **190**(3), 167–180.

French, S. W. & Romanowicz, B. A., 2014. Whole-mantle radially anisotropic shear velocity structure from spectral-element waveform tomography, *Geophysical Journal International*, **199**(3), 1303–1327.

Garnero, E. J. & Lay, T., 1997. Lateral variations in lowermost mantle shear wave anisotropy beneath the north Pacific and Alaska, *Journal of Geophysical Research: Solid Earth*, **102**(B4), 8121–8135.

GFZ Data Services, 1993. GEOFON Data Centre: GEOFON Seismic Network.

Hansen, L. N., Faccenda, M., & Warren, J. M., 2021. A review of mechanisms generating seismic anisotropy in the upper mantle, *Physics of the Earth and Planetary Interiors*, **313**, 106662.

Institut de physique du globe de Paris (IPGP) & École et Observatoire des Sciences de la Terre de Strasbourg (EOST), 1982. Geoscope, french global network of broad band seismic stations.

Instituto de Geofísica, Universidad Nacional Autónoma de México, México, 2024. SSN: Servicio Sismológico Nacional.

Kawai, K. & Geller, R. J., 2010. Waveform inversion for localized seismic structure and an application to D$''$ structure beneath the Pacific, *Journal of Geophysical Research: Solid Earth*, **115**.

Komatitsch, D., Vinnik, L. P., & Chevrot, S., 2010. SHdiff-SVdiff splitting in an isotropic Earth, *Journal of Geophysical Research: Solid Earth*, **115**(B7).

Lay, T. & Young, C. J., 1991. Analysis of seismic SV waves in the core's penumbra, *Geophysical Research Letters*, **18**(8), 1373–1376.

Lekic, V., Cottaar, S., Dziewonski, A., & Romanowicz, B., 2012. Cluster analysis of global lower mantle tomography: A new class of structure and

implications for chemical heterogeneity, *Earth and Planetary Science Letters*, **357-358**, 68–77.

Leng, K., Nissen-Meyer, T., & van Driel, M., 2016. Efficient global wave propagation adapted to 3-D structural complexity: a pseudospectral/spectral-element approach, *Geophysical Journal International*, **207**(3), 1700–1721.

Leng, K., Nissen-Meyer, T., van Driel, M., Hosseini, K., & Al-Attar, D., 2019. AxiSEM3D: broad-band seismic wavefields in 3-D global earth models with undulating discontinuities, *Geophysical Journal International*, **217**(3), 2125–2146.

Link, F., Reiss, M. C., & Rümpker, G., 2022. An automatized XKS-splitting procedure for large data sets: Extension package for SplitRacer and application to the USArray, *Computers & Geosciences*, **158**, 104961.

Liu, K., Elsheikh, A., Lemnifi, A., Purevsuren, U., Ray, M., Refayee, H., Yang, B., Yu, Y., & Gao, S., 2014. A uniform database of teleseismic shear wave splitting measurements for the western and central United States, *Geochemistry, Geophysics, Geosystems*, **15**, 2075–2085.

Long, M. D. & Becker, T., 2010. Mantle dynamics and seismic anisotropy, *Earth and Planetary Science Letters*, **297**, 341–354.

Long, M. D. & Silver, P. G., 2009. Shear Wave Splitting and Mantle Anisotropy: Measurements, Interpretations, and New Directions, *Surveys in Geophysics*, **30**, 407–461.

Meade, C., Silver, P. G., & Kaneshima, S., 1995. Laboratory and seismological observations of lower mantle isotropy, *Geophysical Research Letters*, **22**, 1293–1296.

Mohiuddin, A., D. Long, M., & Lynner, C., 2015. Mid-mantle seismic anisotropy beneath Southwestern Pacific subduction systems and implications for mid-mantle deformation, *Physics of the Earth and Planetary Interiors*, **245**.

Montagner, J.-P., 1998. Where can seismic anisotropy be detected in the Earth's mantle? In boundary layers, *Pure Appl. Geophys.*, **151**, 223–256.

Niu, F. & Perez, A. M., 2004. Seismic anisotropy in the lower mantle: A comparison of waveform splitting of SKS and SKKS, *Geophysical Research Letters*, **31**.

Nowacki, A. & Cottaar, S., 2021. *Toward Imaging Flow at the Base of the Mantle with Seismic, Mineral Physics, and Geodynamic Constraints*, chap. 13, pp. 329–352, American Geophysical Union (AGU).

Nowacki, A., Wookey, J., & Kendall, J.-M., 2010. Deformation of the lowermost mantle from seismic anisotropy., *Nature*, **467**, 1091–1094.

Nowacki, A., Wookey, J., & Kendall, J.-M., 2011. New advances in using seismic anisotropy, mineral physics and geodynamics to understand deformation in the lowermost mantle, *Journal of Geodynamics*, **52**, 205–228.

Parisi, L., Ferreira, A. M. G., & Ritsema, J., 2018. Apparent Splitting of S Waves Propagating Through an Isotropic Lowermost Mantle, *Journal of Geophysical Research: Solid Earth*, **123**, 3909–3922.

Pulliam, J. & Sen, M. K., 1998. Seismic anisotropy in the core—mantle transition zone, *Geophysical Journal International*, **135**, 113–128.

Reiss, M. & Rümpker, G., 2017. SplitRacer: MATLAB Code and GUI for Semiautomated Analysis and Interpretation of Teleseismic Shear-Wave Splitting, *Seismological Research Letters*, **88**, 392 — 409.

RESIF, 1995. RESIF-RLBP French Broad-band network, RESIF-RAP strong motion network and other seismic stations in metropolitan France.

Ritsema, J., Garnero, E., & Lay, T., 1997. A strongly negative shear velocity gradient and lateral variability in the lowermost mantle beneath the pacific, *Journal of Geophysical Research*, **102**, 20395–20412.

Ritsema, J., Lay, T., Garnero, E. J., & Benz, H., 1998. Seismic anisotropy in the lowermost mantle beneath the Pacific, *Geophysical Research Letters*, **25**(8), 1229–1232.

Ritsema, J., Deuss, A., van Heijst, H. J., & Woodhouse, J. H., 2011. S40RTS: a degree-40 shear-velocity model for the mantle from new Rayleigh wave dispersion, teleseismic traveltime and normal-mode splitting function measurements, *Geophysical Journal International*, **184**(3), 1223–1236.

Romanowicz, B. & Wenk, H.-R., 2017. Anisotropy in the deep Earth, *Physics of the Earth and Planetary Interiors*, **269**, 58–90.

Silver, P. G. & Chan, W. W., 1991. Shear wave splitting and subcontinental mantle deformation, *Journal of Geophysical Research: Solid Earth*, **96**, 16429–16454.

Suzuki, Y., Kawai, K., & Geller, R., 2021. Imaging paleoslabs and inferring the Clapeyron slope in D'' beneath the northern Pacific based on high-resolution inversion of seismic waveforms for 3-D transversely isotropic structure, *Physics of the Earth and Planetary Interiors*, **321**, 106751.

Thomas, C. & Kendall, J.-M., 2002. The lowermost mantle beneath northern Asia—II. Evidence for lower-mantle anisotropy, *Geophysical Journal International*, **151**, 296–308.

Trabant, C., Hutko, A. R., Bahavar, M., Karstens, R., Ahern, T., & Aster, R., 2012. Data Products at the IRIS DMC: Stepping Stones for Research and Other Applications.

UC Berkeley Seismological Laboratory, 2014. Northern California Earthquake Data Center.

Vinnik, L., Kosarev, G. L., & Makeyeva, L. I., 1984. Anisotropy of the lithosphere from the observations of SKS and SKKS phases, *Proc. Acad. Sci. USSR*, **278**, 1335–1339.

Vinnik, L., Farra, V., & Romanowicz, B., 1989a. Observational evidence for diffracted SV in the shadow of the Earth's core, *Geophysical Research Letters - GEOPHYS RES LETT*, **16**, 519–522.

Vinnik, L., Farra, V., & Romanowicz, B., 1989b. Azimuthal anisotropy in the earth from observations of SKS at GEOSCOPE and NARS broadband stations, *Bulletin - Seismological Society of America*, **79**, 1542–1558.

Vinnik, L., Romanowicz, B., Le Stunff, Y., & Makeyeva, L., 1995. Seismic anisotropy in the D$''$ layer, *Geophysical Research Letters*, **22**(13), 1657–1660.

Vinnik, L., Bréger, L., & Romanowicz, B., 1998. On the inversion of Sd particle motion for seismic anisotropy in D$''$, *Geophysical Research Letters*, **25**(5), 679–682.

Walpole, J., Wookey, J., Masters, G., & Kendall, J. M., 2014. A uniformly processed data set of SKS shear wave splitting measurements: A global investigation of upper mantle anisotropy beneath seismic stations, *Geochemistry, Geophysics, Geosystems*, **15**, 1991–2010.

Walsh, E., Arnold, R., & Savage, M. K., 2013. Silver and Chan revisited, *Journal of Geophysical Research: Solid Earth*, **118**, 5500–5515.

Wolf, J., 2026. Large-scale flow toward low-velocity anomalies reconciles seismic and geodynamic constraints in the deepest mantle beneath alaska, *Journal of Geophysical Research: Solid Earth*, **131**, e2025JB033063.

Wolf, J. & Long, M. D., 2022. Slab-driven flow at the base of the mantle beneath the northeastern Pacific Ocean, *Earth and Planetary Science Letters*, **594**, 117758.

Wolf, J. & Long, M. D., 2023. Lowermost mantle structure beneath the central Pacific Ocean: Ultralow velocity zones and seismic anisotropy, *Geochemistry, Geophysics, Geosystems*, **24**, e2022GC010853.

Wolf, J., Long, M. D., Leng, K., & Nissen-Meyer, T., 2022. Constraining deep mantle anisotropy with shear wave splitting measurements: Challenges and new measurement strategies, *Geophysical Journal International*, **230**, 507–527.

Wolf, J., Long, M. D., Creasy, N., & Garnero, E., 2023a. On the measurement of Sdiff splitting caused by lowermost mantle anisotropy, *Geophysical Journal International*.

Wolf, J., Long, M. D., Li, M., & Garnero, E., 2023b. Global compilation of deep mantle anisotropy observations and possible correlation with low velocity provinces, *Geochemistry, Geophysics, Geosystems*, **24**(10), e2023GC011070.

Wolf, J., Li, M., Long, M. D., & Garnero, E., 2024a. Advances in mapping lowermost mantle convective flow with seismic anisotropy observations, *Reviews of Geophysics*, **62**, e2023RG000833.

Wolf, J., Long, M. D., & Frost, D. A., 2024b. Ultralow velocity zone and deep mantle flow beneath the Himalayas linked to subducted slab, *Nature Geoscience*, pp. 1–7.

Wolf, J., Becker, T. W., Garnero, E., Liu, K. H., & West, J. D., 2025. Comprehensive global dataset of uniformly processed shear-wave splitting measurements, *Geophysical Journal International*.

Wolf, J., Romanowicz, B. A., & West, J. D., 2026. Splitting constraints in regions with sparse coverage: Uniformly processed PS measurements from a massive global dataset, *Geophysical Journal International*, p. ggaf522.

Wookey, J., Kendall, J.-M., & Rümpker, G., 2005. Lowermost mantle anisotropy beneath the north Pacific from differential S-ScS splitting, *Geophysical Journal International*, **161**, 829–838.

Wysession, M. E., Langenhorst, A., Fouch, M. J., Fischer, K. M., Al-Eqabi, G. I., Shore, P. J., & Clarke, T. J., 1999. Lateral Variations in Compressional/Shear Velocities at the Base of the Mantle, *Science*, **284**(5411), 120–125.

Yuan, K. & Beghein, C., 2014. Three-dimensional variations in Love and Rayleigh wave azimuthal anisotropy for the upper 800km of the mantle, *Journal of Geophysical Research: Solid Earth*, **119**, 3232–3255.